

# Planetary ENA Imaging: Venus and a comparison with Mars

H. Gunell<sup>a,\*</sup>, M. Holmström<sup>a</sup>, H. K. Biernat<sup>b</sup>, and  
N. V. Erkaev<sup>c</sup>

<sup>a</sup>*Swedish Institute of Space Physics, Box 812, SE-981 28 Kiruna, Sweden*

<sup>b</sup>*Space Research Institute, Austrian Academy of Sciences, Schmiedlstrasse 6,  
A-8042 Graz, Austria*

<sup>c</sup>*Institute of Computational Modelling, Russian Academy of Sciences,  
660036 Krasnoyarsk 36, Russia*

---

## Abstract

We present simulated images of energetic neutral atoms (ENAs) produced in charge exchange collisions between solar wind protons and neutral atoms in the exosphere of Venus, and make a comparison with earlier results for Mars. The images are found to be dominated by two local maxima. One produced by charge exchange collisions in the solar wind, upstream of the bow shock, and the other close to the dayside ionopause. The simulated ENA fluxes at Venus are lower than those obtained in similar simulations of ENA images at Mars at solar minimum conditions, and close to the fluxes at Mars at solar maximum. Our numerical study shows that the ENA flux decreases with an increasing ionopause altitude. The influence of the Venus nighttime hydrogen bulge on the ENA emission is small.

*Key words:*

*PACS:* 52.65.Kj, 96.30.Ea, 96.30.Gc, 96.35.Hv

---

## 1 Introduction

Energetic neutral atoms (ENAs) are produced in charge exchange collisions between solar wind protons and neutral atoms in the upper part of the atmospheres of the planets. ENA images of Earth's magnetosphere have been

---

\* Corresponding author

*Email address:* herbert.gunell@physics.org (H. Gunell).

obtained by instruments on the IMAGE satellite (Burch et al., 2001). Holmström et al. (2002) simulated images of ENAs produced by the interaction between the solar wind and Mars through the integration of the ENA production along lines of sight to a virtual ENA instrument.

The ASPERA-4 instrument onboard the European Space Agency's (ESA) Venus Express mission will provide ENA images of the Venus-solar wind interaction region. ASPERA-4 is identical to the ASPERA-3 instrument (Barabash et al., 2004) on ESA's Mars Express mission.

In this work ENA images of the region where the solar wind interacts with Venus' atmosphere are calculated. To simulate an ENA image one needs a model for how the density of the neutral gas species varies as a function of the spatial coordinates, a model for the plasma density and temperature, and knowledge of the cross sections for charge exchange collisions between protons and the neutral gas.

Due to the scarcity of in situ measurements the ionopause altitude at Venus is not well known for solar minimum conditions (Luhmann, 1992). It is thought to vary with the solar cycle, but since all in situ measurements were made during solar maximum conditions this variation is still unconfirmed. We investigate the ENA emissions as a function of ionopause distance by scaling the ionopause altitude in the plasma model through the range from 250 km to 500 km. The ionopause is thought to be close to the lower end of that range at solar minimum because of the lower ionospheric pressure (Luhmann, 1992).

The plasma model used in this work is a semi-analytical MHD model (Biernat et al., 1999, 2000, 2001), and is briefly described in section 2. The neutral gas density model is based on published data from measurement and is described in section 3. The ENA images are then generated by evaluating line of sight integrals in the same way as it has previously been done to simulate ENA images of the Martian environment (Holmström et al., 2002). The ENA results are presented in section 4. In section 5 the results from Venus are compared to ENA simulations of the interaction between the solar wind and Mars. Conclusions and implications are discussed in section 6.

## 2 Plasma model

The model for the plasma flow around Venus that is used here is a semi-analytical MHD calculation scheme that was developed by Biernat et al. (1999, 2000), and extended to include mass loading (Biernat et al., 2001). It is semi-analytical in that it numerically finds steady state solutions to the MHD equations, assuming analytical expressions for the shape of the ionopause and bow

shock, and for the spatial variation of the total pressure. The input parameters of the solar wind are shown in table 1, and the boundary conditions were described by Biernat et al. (2001). The MHD approximation is valid since the gyro radius is small compared to the relevant length scales. The gyro radius for solar wind protons is less than 1% of the radius of Venus.

The solar wind is loaded by heavy ions that are created in the vicinity of Venus through photo-ionisation, charge exchange and electron impact ionisation. These processes are not self-consistently taken into account in the MHD calculations. Instead mass loading is included through an ion source function that falls off exponentially with altitude, and has a single scale height. This source function serves as an approximation of the total ion production from photo-ionisation, charge exchange and electron impact ionisation (Biernat et al., 2001; Kallio et al., 1998). The ion source function for mass loading is

$$q = q_0 \exp(-(r - L_0)/H_0),$$

where  $r$  is the distance to the centre of Venus,  $L_0$  is the planetocentric distance of the ionopause at the subsolar point,  $H_0 = 400$  km is the scale height for mass loading, and  $q_0$  is the dimensionless mass loading parameter. In this paper  $q_0 = 1$  has been used.

The MHD model is used to calculate the plasma density, temperature, and bulk velocity in a region on the dayside of Venus, between the ionopause and the bow shock. To define the flow at all positions, these values are then extrapolated to the downstream region. Inside the ionopause the ion density is assumed to be zero. Outside the bow shock undisturbed solar wind parameters are assumed. We use a coordinate system with the origin at the centre of Venus, and where the  $x$ -axis is along the Venus-sun line; the  $z$ -axis perpendicular to the ecliptic plane and directed to the north; and the  $y$ -axis completes the right-handed system. The  $x$ -component of the plasma velocity in the different regions is shown in Fig. 1. The calculations were performed in the  $xz$ -plane, and to obtain plasma data outside that plane cylindrically symmetric around the  $x$ -axis has been assumed.

### 3 Neutral model

The model of the neutral gas density used in this work is based on data found in the literature, and has been extrapolated to higher altitudes using a Chamberlain exosphere (Chamberlain and Hunten, 1987). Hot and thermal populations of atomic hydrogen and atomic oxygen have been included. Although the helium density in some regions is comparable to the densities of oxygen and hydrogen it has not been included, because the cross section for charge exchange collisions between protons and helium is negligible in comparison

with the corresponding cross sections for proton-hydrogen and proton-oxygen collisions (Kallio et al., 1997).

Brinton et al. (1980) derived hydrogen densities from measurements made by the Pioneer Venus orbiter, and showed that there is a high density bulge on the nightside with the maximum shifted toward dawn. To extend Brinton’s measurements to regions away from the equator Rodriguez et al. (1984) divided Venus into seven zones where the density is constant within each zone. We model the density of thermal hydrogen by following Rodriguez’s model of the density and temperature at the exobase, and use a Chamberlain exosphere to extrapolate to higher altitudes. We only include the terms of Chamberlain’s partition function that involve ballistic and escaping orbits, because particles on satellite orbits are thought to be lost in the bulge (Rodriguez et al., 1984).

We model the hot hydrogen density by fitting a function of the form

$$N(r) = e^{a_1 r + a_2 + a_3/r}$$

to the exospheric densities calculated by Rodriguez et al. (1984). They published results for solar zenith angles  $0^\circ$ ,  $90^\circ$ , and  $180^\circ$ . For other solar zenith angles we use linear interpolation to estimate the hot hydrogen density. The coefficients  $a_1$ ,  $a_2$ , and  $a_3$ , are given in Table 2

Thermal oxygen is modelled using an analytical fit to the “standard case” of Mengel et al. (1989) at 170 km altitude, and using a Chamberlain exosphere for higher altitudes. The temperature is fitted by the function  $T = (314 - 44.1\theta^2)$  K when  $\theta < 1.9284$  and  $T = 150$  K for  $\theta \geq 1.9284$ , where  $\theta$  is the solar zenith angle. The density at 170 km altitude is modelled by

$$N = 10^{14.5 + 0.46 \cos(\theta)}.$$

On the dayside the density of the hot oxygen component is  $7.5 \times 10^{10} \text{m}^{-3}$  at 200 km altitude, and the temperature is 6400 K (McElroy et al., 1982). On the nightside the density and temperature are  $2 \times 10^9 \text{m}^{-3}$  at 300 km altitude and 4847 K respectively (Nagy et al., 1981). These values are then extrapolated using a Chamberlain exosphere.

The resulting hydrogen and oxygen densities at the sub-solar and anti-solar points are shown in Fig. 2. The division of the planet in different zones introduces sharp changes in the neutral densities, particularly at the terminator. This will have little influence on the ENA images, which are the result of integration along lines of sight. The response of Venus’ neutral upper atmosphere to solar cycle variations is small (Keating et al., 1985), and this model applies to both solar minimum and maximum conditions.

## 4 ENA images and fluxes

The ENA images were calculated by integrating the ENA production along lines of sight, as was described by Holmström et al. (2002). The energy dependent cross sections for charge exchange collisions between protons and hydrogen and between protons and oxygen were taken from Kallio et al. (1997). The integration is limited outward to a sphere of radius  $10R_v$  centred at Venus, where  $R_v = 6051.8$  km is the radius of Venus. Only ENAs with energies above 50 eV are considered here, since the contribution from lower energies is small (Holmström et al., 2002) and because the assumption that a newly produced ENA has the same momentum as the incident proton is not valid for energies lower than approximately 50 eV (Hodges and Breig, 1996).

We have assumed that the atmosphere is an impenetrable obstacle up to 250 km altitude and that the atmosphere is ENA thin above that altitude. A calculation similar to that performed for the Martian atmosphere by Kallio et al. (1997) confirms this. Only 13 % of ENAs travelling along a straight line with a closest distance of 250 km to Venus' surface are lost. For lines with a closest approach of 200 km the loss is 82 % and at 300 km it is 1 %. The integration, in this calculation, was carried out for the part of that straight line which falls within a Venus-centred sphere with a radius of  $6R_v$ .

Six ENA images from vantage points in the  $xz$ -plane at different solar zenith angles are shown in Fig. 3. The vantage points are located three Venus radii from the centre of Venus, and the solar zenith angles are  $80^\circ$ ,  $100^\circ$ ,  $120^\circ$ ,  $140^\circ$ ,  $160^\circ$ , and  $180^\circ$  for the six images respectively. The ENA flux is shown in units of  $\text{sr}^{-1}\text{m}^{-2}\text{s}^{-1}$ . The centre of each image corresponds to the direction looking straight toward the centre of Venus. The white circle shows the location of Venus' surface. For all six images the ionopause altitude is 250 km at the subsolar point.

In the images from solar zenith angles between  $100^\circ$  and  $140^\circ$  the ENA flux has two local maxima: one on the dayside of Venus and the other in the direction of the sun. The latter maximum is produced upstream of the bow shock by charge exchange collisions between the protons in the unperturbed solar wind and atoms in the exosphere of Venus. At solar zenith angle  $\theta = 80^\circ$  the Sun is outside the picture, at  $\theta = 160^\circ$  the two maxima overlap, and at  $\theta = 180^\circ$  the Sun is occulted by Venus.

Fig. 4 shows ENA images calculated using three different ionopause altitudes, namely 250 km, 375 km, and 500 km at the subsolar point. The vantage point is in the  $xz$ -plane at  $3R_v$  planetocentric distance with a solar zenith angle of  $110^\circ$  for all three images.

The ENA flux from the local emission maximum near the planet decreases

with increasing ionopause altitude, since with a higher ionopause altitude the protons pass through a region with lower neutral density. It can also be seen in Fig. 4 that the maximum moves slightly outward from the planet as the ionopause altitude increases. The maximum that corresponds to ENAs produced upstream in the solar wind remains unchanged by changes in the ionopause altitude. Fig. 5 shows the maximum ENA flux as a function of ionopause altitude. The ENAs from upstream of the bow shock have been excluded in the calculation and only the maximum near the planet is taken into account. The curve shows the maximum ENA flux as measured from a vantage point in the  $xz$ -plane  $3R_v$  away from the centre of Venus. For each ionopause altitude the solar zenith angles from  $90^\circ$  to  $130^\circ$  have been scanned through in steps of  $1^\circ$ , finding the maximum flux for each step. The decrease of the maximum ENA flux with ionopause altitude is a result of the decrease in neutral gas density with altitude. As the ionopause is scaled to higher altitudes the bulk proton flow passes through regions with lower neutral gas density.

Fig. 6 shows the ENA production rate per unit volume in cylindrical coordinates for an ionopause altitude of 400 km in units of  $\text{m}^{-3}\text{s}^{-1}$ . It is seen from a comparison of Fig. 6 with Fig. 1 that the region with significant ENA production coincides with the region where we have calculated MHD data. The total hydrogen ENA production rate integrated over the whole region shown in Fig. 6 is  $5.6 \times 10^{24} \text{ s}^{-1}$ . For an ionopause altitude of 250 km the total production rate is  $8.1 \times 10^{24} \text{ s}^{-1}$ .

The rate of ENA production inside a sphere with a radius of  $3R_v$ , centred on Venus, is  $5.3 \times 10^{24} \text{ s}^{-1}$ . This value was calculated by integrating over the volume inside the sphere but outside the obstacle boundary, i.e., over the region between a Venus-centred sphere with radius  $R_v + 250 \text{ km}$ , the obstacle, and the  $3R_v$  sphere mentioned above. The escape rate of ENAs out of this sphere was calculated by integrating the ENA flux across the surface of the  $3R_v$  sphere. This escape rate is  $4.0 \times 10^{24} \text{ s}^{-1}$ . The rate of ENA precipitation on the obstacle boundary, calculated by integrating the ENA flux across this boundary, is  $1.2 \times 10^{24} \text{ s}^{-1}$ , all for a subsolar ionopause altitude of 400 km. When the altitude of the subsolar ionopause is 250 km the ENA production rate inside the sphere is  $7.8 \times 10^{24} \text{ s}^{-1}$ . The escape and precipitation rates are  $5.6 \times 10^{24} \text{ s}^{-1}$  and  $2.2 \times 10^{24} \text{ s}^{-1}$  respectively. These rates are also shown in table 3.

The left and middle panels of Fig. 7 show ENA images from vantage points three  $R_v$  from the centre of Venus, located on the positive  $y$ -axis (left panel) and on the negative  $y$ -axis (middle panel). The colour scales are logarithmic in these two images. The effect of the nighttime hydrogen bulge can be seen in the left panel as an area with an increased flux of hydrogen ENAs on the nightside close to the nadir direction. This increase is absent when Venus is viewed from

the opposite direction as is shown in the middle panel. The right panel of Fig. 7 shows the difference between the left and the middle panels. Thus the image in the right panel corresponds to the additional flux that is caused by the presence of the bulge. The maximum contribution from the bulge, taken as the flux at the brightest pixel in the right panel, is  $1.7 \times 10^8 \text{ sr}^{-1} \text{ m}^{-2} \text{ s}^{-1}$ . This should then be compared to the maximum flux observed in the left and middle panels which is  $3.1 \times 10^{10} \text{ sr}^{-1} \text{ m}^{-2} \text{ s}^{-1}$ . We thus conclude that the contribution to the ENA images from the bulge is small, because most of the bulge is located where the proton flux is small.

## 5 Mars–Venus comparison

The numerical values reported in this section are also shown in table 3. The ENA escape rate, calculated as the flux out from a sphere of radius  $3R_v$ , centred at Venus, of ENAs produced inside it, was  $5.3 \times 10^{24} \text{ s}^{-1}$ , with an ionopause altitude of 250 km. The corresponding number for Mars, using a  $3R_m$  sphere, is  $1.5 \times 10^{25} \text{ s}^{-1}$  (Holmström et al., 2002), i.e., the escape rate at Mars is 2.8 times that at Venus. The precipitation rates are  $2.2 \times 10^{24} \text{ s}^{-1}$  and  $1.4 \times 10^{24} \text{ s}^{-1}$  for Venus and Mars respectively. Thus the precipitation rate at Venus is higher than at Mars. This is not unexpected because Venus is a larger planet, and the Venusian ENA production region is located closer to Venus than the Martian ENA production region is to Mars, which is seen in Fig. 8. The left panel of Fig. 8 shows an ENA image of Mars (Gunell et al., 2004), that is based on an MHD model for the plasma flow (Ma et al., 2002). The solar wind parameters used by Ma et al. (2002) are shown in table 1. The right panel of Fig. 8 shows an ENA image of Venus. Both images are from vantage points at solar zenith angle  $120^\circ$  and a planetocentric distance of three radii of the respective planet.

Three different simulation models for Mars, one empirical, one MHD, and one hybrid model, are compared by Gunell et al. (2004). The differences between the models and the implications for ENA imaging are discussed in detail in that paper. Here we shall compare the results of our present MHD model for Venus with the results of the MHD model for Mars. The MHD model for Mars yields a total hydrogen ENA production rate of  $2.4 \times 10^{25} \text{ s}^{-1}$ . The production rate obtained here for Venus, with the ionopause at 250 km altitude, is  $7.8 \times 10^{24} \text{ s}^{-1}$ , i.e., one third of the production rate for Mars. Both Holmström et al. (2002) and Gunell et al. (2004) used neutral density profiles for Mars at solar minimum conditions. At solar maximum the density of neutral hydrogen in the exosphere at Mars is lower, which leads to a lower ENA production rate. Hydrogen is the most important species for ENA production at Mars. The total ENA production rate for Mars computed using the MHD model (Ma et al., 2002) for the plasma flow and solar maximum neutral gas densities

(Krasnopolsky and Gladstone, 1996; Kallio et al., 1997) is  $5.1 \times 10^{24} \text{ s}^{-1}$ . The ENA production at Venus is thus approximately the same as at Mars at solar maximum conditions, but lower than at Mars at solar minimum. For Venus the response of the upper atmosphere to changes in the solar activity is small (Keating et al., 1985), and therefore we do not distinguish between the solar maximum and minimum cases for Venus.

The ENA flux and production rates at Venus are lower than at Mars even though the solar wind flux is greater at Venus. The reason for this is that the neutral gas density at relevant heights is lower in Venus' than Mars' exosphere. The neutral density falls off more rapidly with altitude at Venus, because of the larger mass of that planet, which is 7.5 times greater than the mass of Mars. The dominant contribution to the neutral density at high altitudes at Mars during solar minimum conditions is the large hydrogen corona (Krasnopolsky and Gladstone, 1996). The hydrogen density at Mars is greater than that at Venus everywhere above the exobase, and hydrogen is by far the most important species for ENA production at Mars (Holmström et al., 2002).

To show the contributions from different regions, and to illustrate the differences between Venus and Mars, we examine the contributions from different positions along a line of sight. Fig. 9 shows, in the three panels on the left side, from top to bottom, the total neutral gas density, the plasma flux, and the rate of ENA production in the direction toward the vantage point, as functions of distance along the line of sight from the vantage point. The ENA production rate, when integrated along the line of sight, gives the differential ENA flux that is shown in the ENA images. The right panel shows the lines of sight along for which the different quantities are plotted in the left panels. The filled red circle represents Mars and the yellow Venus. The vantage points are at solar zenith angle  $80^\circ$  and a planetocentric distance of three radii of the respective planet. The direction of the lines of sight corresponds to the direction of the pixel with the maximum flux of an ENA image from that vantage point. Because the topology of the plasma flow is different at Venus and Mars the directions of the maximum flux is also different at the two planets. The higher exospheric density at Mars is what makes the ENA flux at Mars greater than at Venus, as is seen in the top left panel. Although the solar wind density is higher at Venus, the flux in the relevant region, i.e., close to the planet, is similar to that at Mars (middle left panel). The bulk speed of the plasma is slowed down near the planet, and the line of sight that yields the highest differential flux is farther away from the planet at Mars than at Venus.

It is interesting to compare the results obtained here with the results of Fok et al. (2004). Although their parameters are not exactly the same as ours they are at least similar. Fok et al. (2004) took the effect of space craft motion into account. We do not. Since we are considering ENAs with energies above

50 eV this amounts only to a small correction in our case. We have calculated ENA images from the same vantage points that were used in Fig. 5 of (Fok et al., 2004), and we obtained a maximum ENA flux of  $3.8 \times 10^{10} \text{ sr}^{-1} \text{ m}^{-2} \text{ s}^{-1}$  from the interaction region between the dayside ionopause and the bow shock, which should be compared to the  $1.4 \times 10^{10} \text{ sr}^{-1} \text{ m}^{-2} \text{ s}^{-1}$  obtained by in the left panel of their Fig. 5, which shows an ENA image from Fok et al. (2004) the vantage point  $(x, y, z) = (0.41R_v, 0, 1.59R_v)$ . In the right panel of Fig. 5 of Fok et al. (2004), which shows an ENA image from the vantage point  $(x, y, z) = (0, 1.63R_v, 0.31R_v)$ , their maximum flux is  $1.2 \times 10^{11} \text{ sr}^{-1} \text{ m}^{-2} \text{ s}^{-1}$ , and we obtain  $5.3 \times 10^{10} \text{ sr}^{-1} \text{ m}^{-2} \text{ s}^{-1}$ . Both models yield ENA fluxes of the same order of magnitude. In one case the flux calculated here is larger and in the other case it is smaller than that calculated by Fok et al. (2004). The difference could be caused by differences in the models of the neutral density and the plasma flow, but it can also be an effect of the finite resolution of the figures and that Fok et al. (2004) include ENAs with energies down to 2 eV, whereas our lower energy limit is 50 eV. We conclude that the two models are in reasonable agreement considering the uncertainties of the models. Real measurements will be required to determine between them, or indeed to say anything conclusively about the accuracy of the models.

## 6 Conclusions

We have simulated ENA images of the Venus-solar wind interaction region, and studied the dependence of the ENA flux on the ionopause position by scaling the plasma results of the MHD calculation. The main contribution to the ENA flux observed in the ENA images stems from a region of space between the ionopause and the bow shock on the dayside of the planet.

The maximum flux observed at  $3R_v$  planetocentric distance, coming from the interaction region on the dayside of Venus is  $5.8 \times 10^{10} \text{ sr}^{-1} \text{ m}^{-2} \text{ s}^{-1}$ , which occurs for the lowest ionopause altitude, i.e., 250 km. The ENAs that are produced in the solar wind upstream of the bow shock are not included in this number. For higher ionopause altitudes the ENA flux decreases, and is below  $3.8 \times 10^{10} \text{ sr}^{-1} \text{ m}^{-2} \text{ s}^{-1}$ , when the subsolar ionopause is at 400 km altitude. The corresponding number for Mars at solar minimum conditions, computed by Holmström et al. (2002) is about  $3 \times 10^{11} \text{ sr}^{-1} \text{ m}^{-2} \text{ s}^{-1}$ , which is five times larger than the value obtained for Venus with an ionopause altitude of 250 km. The ENA production rate at Mars at solar maximum conditions is about the same as that at Venus.

In comparison with Mars the ENA fluxes and the total ENA production rates at Venus are lower. This is explained by the neutral corona which extends further into space at Mars than at Venus. Thus the neutral gas density at

Mars is higher than at Venus in the altitude range that is important for ENA production. It can also be seen in the ENA images that the ENA production is concentrated closer to the planet at Venus than at Mars.

The effect of the nighttime hydrogen bulge (Brinton et al., 1980) on the ENA images was found to be small, due to the low proton flux at the low altitudes where the bulge is dominant.

At the present time no measured ENA images of Venus and Mars are available. Also the measurements of the components that determine the ENA flux and the morphology of the images, i.e, the neutral density and the density, temperature, and bulk velocity of the plasma, are quite scarce. Furthermore the solar wind parameters vary substantially with time. This means that there are considerable uncertainties in the input parameters of the numerical calculations of ENA images, due to the uncertainties in the solar wind parameters and in the neutral densities of the upper atmospheres. It also means that the output of a solar wind-planetary interaction model, i.e., plasma density, temperature, and bulk velocity in the vicinity of the planet, cannot be checked by comparison with measured data. An MHD model neglects all kinetic and finite gyro radius effects, which may turn out to be important for ENA imaging. Hybrid models, which treat the electrons as a fluid and the ions as particles, take kinetic and finite gyro radius effects into account, but instead suffer from lower accuracy, since limited computer resources requires the use of large grid cell size and a small number of particles. The differences between different models and the implications for ENA imaging is discussed further by Gunell et al. (2004).

## 7 Acknowledgments

This work was supported by the Swedish National Space Board; the FWF Austrian Science Fund, project P17100-N08; grant No 01-05-65070 from the Russian Foundation of Basic Research; and grant E02-8.0-22 from the Russian Ministry of Higher Education.

## References

- Barabash, S., Lundin, R., Andersson, H., et al., 2004. ASPERA-3: Analyser of space plasmas and energetic ions for mars express. ESA Special Publication, SP-1240, in press.
- Biernat, H. K., Erkaev, N. V., Farrugia, C. J., 1999. Aspects of MHD flow about Venus. *Journal of Geophysical Research* 104, 12617–12626.
- Biernat, H. K., Erkaev, N. V., Farrugia, C. J., 2000. MHD effects in the Venus magnetosheath. *Advances in Space Research* 26, 1587–1591.

- Biernat, H. K., Erkaev, N. V., Farrugia, C. J., 2001. MHD effects in the Venus magnetosheath including mass loading. *Advances in Space Research* 28, 833–839.
- Brinton, H. C., Taylor, Jr., H. C., Niemann, H. B., Mayr, H. G., Nagy, A. F., Cravens, T. E., Strobel, D. F., 1980. Venus nighttime hydrogen bulge. *Geophysical Research Letters* 7, 865–868.
- Burch, J. L., Mende, S. B., Mitchell, D. G., Moore, T. E., Pollock, C. J., Reinisch, B. W., Sandel, B. R., Fuselier, S. A., Gallagher, D. L., Green, J. L., Perez, J. D., Reiff, P. H., 2001. Views of Earth's magnetosphere with the IMAGE satellite. *Science* 291 (5504), 619–624.
- Chamberlain, J. W., Hunten, D. M., 1987. *Theory of planetary atmospheres*, 2nd Edition. Academic Press, inc., San Diego, California.
- Fok, M.-C., Moore, T. E., Collier, M. R., Tanaka, T., 2004. Neutral atom imaging of solar wind interaction with the Earth and Venus. *Journal of Geophysical Research* 109 (A1), A01206, doi:10.1029/2003JA010094.
- Gunell, H., Holmström, M., Barabash, S., Kallio, E., Janhunen, P., Nagy, A. F., Ma, Y., 2004. Planetary ENA imaging: II. effects of different interaction models for mars. Submitted to *Planetary and Space Science*.
- Hodges, Jr., R. R., Breig, E. L., 1996. Ionosphere - exosphere coupling through charge exchange and momentum transfer in hydrogen-proton collisions. *Journal of Geophysical Research* 96 (A5), 7697–7708.
- Holmström, M., Barabash, S., Kallio, E., 2002. Energetic neutral atoms at Mars I: Imaging of solar wind protons. *Journal of Geophysical Research* 107 (A10), 1277, doi:10.1029/2001JA000325.
- Kallio, E., Luhmann, J. G., Barabash, S., 1997. Charge exchange near Mars: The solar wind absorption and energetic neutral atom production. *Journal of Geophysical Research* 102, 22183–22197.
- Kallio, E., Luhmann, J. G., Lyon, J. G., 1998. Magnetic field near Venus: A comparison between Pioneer Venus Orbiter magnetic field observations and an MHD simulation. *Journal of Geophysical Research* 103, 4723–4737.
- Keating, G. M., Bertaux, J. L., Bougher, S. W., Cravens, T. E., Dickinson, R. E., Hedin, A. E., Krasnopolsky, V. A., Nagy, A. F., Nicholson III, J. Y., Paxton, L. J., von Zahn, U., 1985. Models of Venus neutral upper atmosphere: structure and composition. *Advances in Space Research* 5 (11), 117–171.
- Krasnopolsky, V. A., Gladstone, G. R., 1996. Helium on Mars: EUVE and PHOBOS data and implications for Mars' evolution. *Journal of Geophysical Research* 101 (A7), 15765–15772.
- Luhmann, J. G., 1992. Comparative studies of the solar wind interaction with weakly magnetized planets. *Advances in Space Research* 12 (9), 191–203.
- Ma, Y., Nagy, A. F., Hansen, K. C., DeZeeuw, D. L., Gombosi, T. I., 2002. Three-dimensional multispecies MHD studies of the solar wind interaction with Mars in the presence of crustal fields. *Journal of Geophysical Research* 107 (A10), 1282, doi:10.1029/2002JA009293.
- McElroy, M. B., Prather, M. J., Rodriguez, J. M., 1982. Loss of oxygen from

- Venus. *Geophysical Research Letters* 9, 649–651.
- Mengel, J. G., Stevens-Rayburn, D. R., Mayr, H. G., Harris, I., 1989. Non-linear three dimensional spectral model of the Venusian thermosphere with super-rotation–II. temperature composition and winds. *Planetary and Space Science* 37, 707–722.
- Nagy, A. F., Cravens, T. E., Yee, J.-H., Stewart, A. I. F., 1981. Hot oxygen atoms in the upper atmosphere of Venus. *Geophysical Research Letters* 8, 629–632.
- Rodriguez, J. M., Prather, M. J., McElroy, M. B., 1984. Hydrogen on Venus: exospheric distribution and escape. *Planetary and Space Science* 32, 1235–1255.

Table 1

Solar wind parameters used in the MHD simulations of Venus in this work, and those used by Ma et al. (2002) and Holmström et al. (2002) for Mars.

	Venus	Mars (Ma et al.)	Mars Holmström et al.
Electron number density	$1.5 \times 10^7 \text{m}^{-3}$	$4 \times 10^6 \text{m}^{-3}$	$2.5 \times 10^6 \text{m}^{-3}$
Solar wind speed	$4.4 \times 10^5 \text{m/s}$	$5 \times 10^5 \text{m/s}$	$4 \times 10^5 \text{m/s}$
Solar wind temperature	$2 \times 10^5 \text{K}$	$1.75 \times 10^5 \text{K}$	$1.2 \times 10^5 \text{K}$
Solar wind magnetic field	$1.2 \times 10^{-8} \text{T}$	$3 \times 10^{-9} \text{T}$	

Table 2

Coefficients for the analytical fit of the hot hydrogen density profiles

	$a_1/\text{km}^{-1}$	$a_2$	$a_3/\text{km}$
Noon	$-6.2625 \times 10^{-5}$	15.4817	$3.6414 \times 10^4$
Terminator	$-8.4607 \times 10^{-5}$	15.9944	$2.9743 \times 10^4$
Midnight	$-6.2309 \times 10^{-5}$	15.2723	$4.3781 \times 10^4$

Table 3

A comparison of some aspects of the results from Venus and Mars. Values for Venus are given for ionopause altitudes 250 km and 400 km respectively. Venus' upper atmosphere is approximately the same independent of the solar cycle. The values for Mars from Holmström et al. (2002) are all for solar minimum conditions. Values from the MHD simulation of Mars were taken from Gunell et al. (2004). "Max. flux" refers to the maximum flux in an ENA image of the interaction region downstream of the bow shock. Solar minimum and maximum conditions are denoted by "min" and "max" respectively.

	Venus IP 250 km	Venus IP 400 km	Mars Holmström	Mars MHD (Gunell)	unit
Production rate	$7.8 \cdot 10^{24}$	$5.6 \cdot 10^{24}$	$1.7 \cdot 10^{25}$	$\left\{ \begin{array}{l} 2.4 \cdot 10^{25}, \text{ min} \\ 5.1 \cdot 10^{24}, \text{ max} \end{array} \right.$	$\text{s}^{-1}$
Escape rate	$5.3 \cdot 10^{24}$	$4.0 \cdot 10^{24}$	$1.5 \cdot 10^{25}$		$\text{s}^{-1}$
Precip. rate	$2.2 \cdot 10^{24}$	$1.2 \cdot 10^{24}$	$1.4 \cdot 10^{24}$		$\text{s}^{-1}$
Max. flux	$5.8 \cdot 10^{10}$	$3.8 \cdot 10^{10}$	$3 \cdot 10^{11}$	$1.1 \cdot 10^{11}, \text{ min}$	$\text{sr}^{-1} \text{m}^{-2} \text{s}^{-1}$

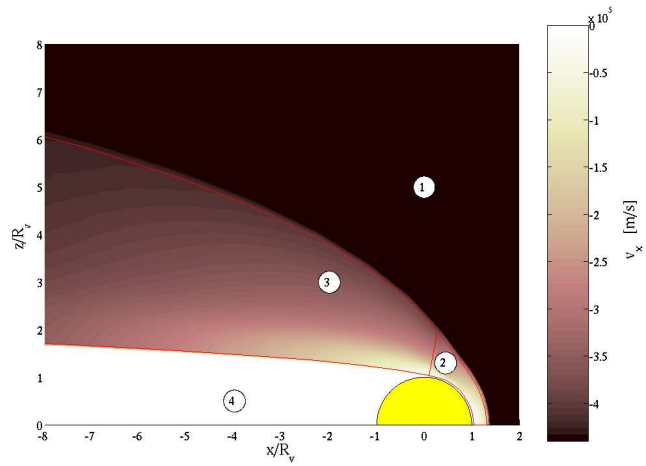


Fig. 1. Proton velocity  $v_x$  shown in the  $xz$ -plane. For ENA imaging purposes rotational symmetry around the  $x$ -axis is assumed. The numbered regions are: (1) the unperturbed solar wind; (2) the region between the ionopause and the bow shock where MHD simulations are performed; (3) a region where extrapolated plasma data was used; and (4) the wake behind Venus where zero plasma density has been assumed.

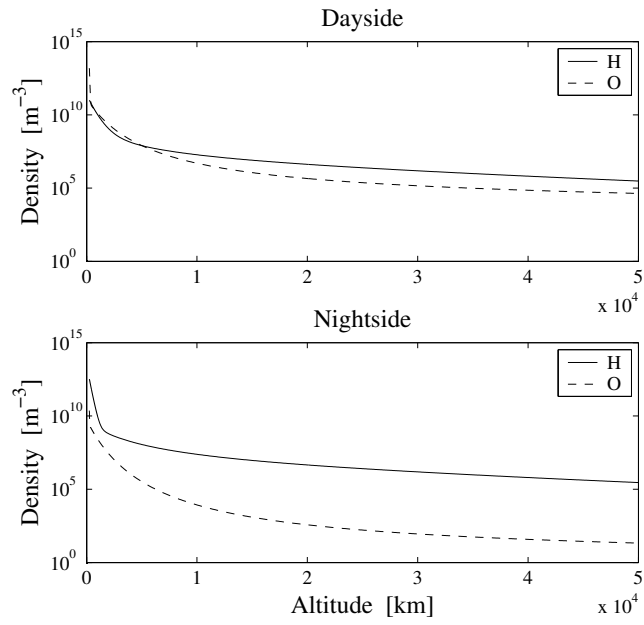


Fig. 2. Neutral densities as functions of altitude for atomic hydrogen and oxygen at the sub-solar (upper panel) and anti-solar (lower panel) points.

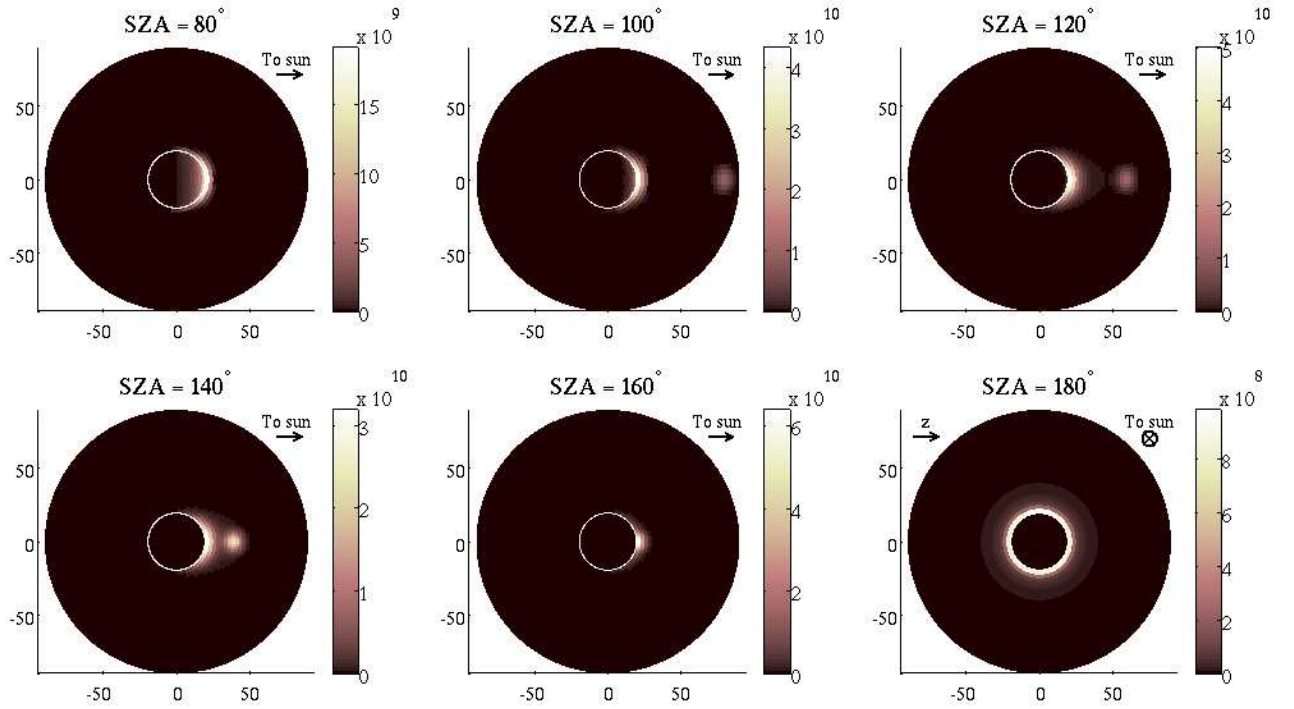


Fig. 3. ENA images of Venus from vantage points  $3R_v$  from Venus (planetocentric distance) and solar zenith angles  $\theta = 80^\circ, 100^\circ, 120^\circ, 140^\circ, 160^\circ,$  and  $180^\circ$ . The ENA flux is shown in units of  $\text{sr}^{-1}\text{m}^{-2}\text{s}^{-1}$ , and the axes show the polar angle in degrees. The altitude of the ionopause is 250 km at the subsolar point. The dominant contribution to the ENA flux comes from a region between the ionopause and the bow shock on the day-side of Venus, except in the lower right panel where  $\theta = 180^\circ$ , and this region is occulted by Venus. The second maximum toward the right side of the images with  $100^\circ < \theta < 140^\circ$ , is produced upstream of the bow shock in the solar wind. Each image has its own colour scale.

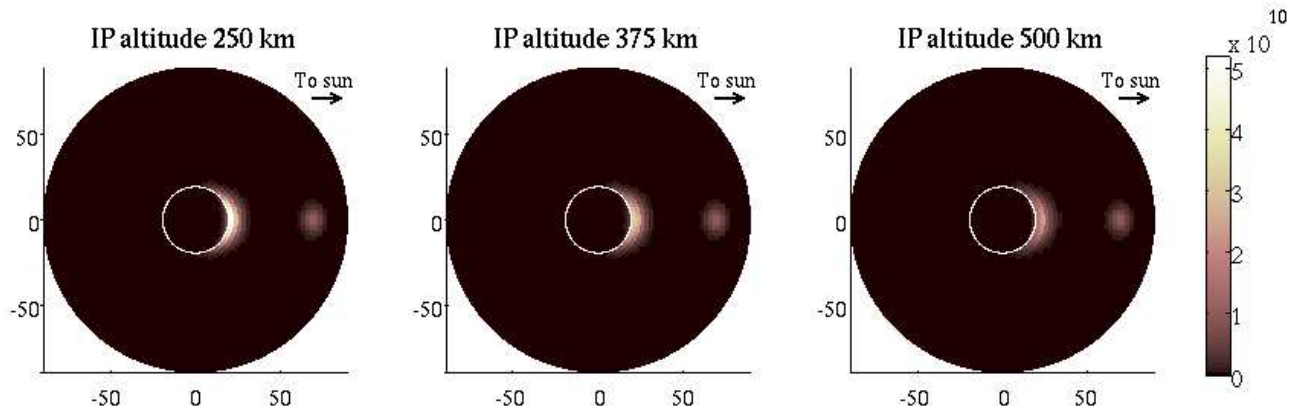


Fig. 4. ENA images with 250 km ionopause altitude (left panel), 375 km (middle panel), and 500 km (right panel). The vantage point is in the  $xz$ -plane at  $3R_v$  planetocentric distance with a solar zenith angle of  $110^\circ$  for all three images. The ENA flux decreases with an increasing ionopause altitude, i.e. going from the left to the right panel. The maximum also moves slightly away from the planet with the increasing ionopause altitude.

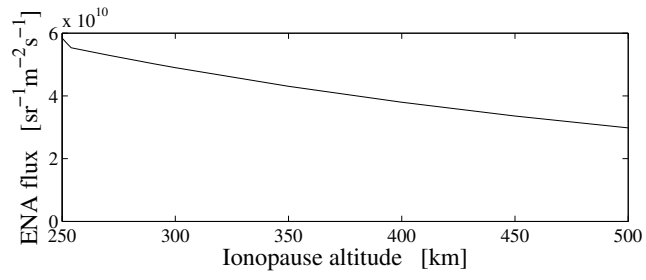


Fig. 5. Maximum flux, as observed by a virtual instrument in the  $xz$ -plane  $3R_v$  from the centre of Venus, shown as a function of the subsolar ionopause altitude. The decrease of the maximum ENA flux with ionopause altitude is a result of the decrease in neutral gas density with altitude.

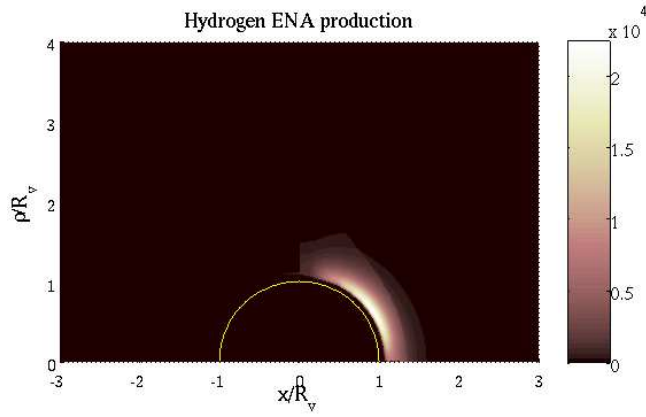


Fig. 6. ENA production rate for an ionopause altitude of 400 km. The cylindrical coordinate  $\rho = \sqrt{y^2 + z^2}$  is the distance to the Venus-sun line. The production rate is shown in units of  $\text{m}^{-3}\text{s}^{-1}$ . The total hydrogen ENA production rate integrated over the whole region shown in this figure is  $5.6 \times 10^{24} \text{ s}^{-1}$ . For an ionopause altitude of 250 km the total production rate is  $8.1 \times 10^{24} \text{ s}^{-1}$ .

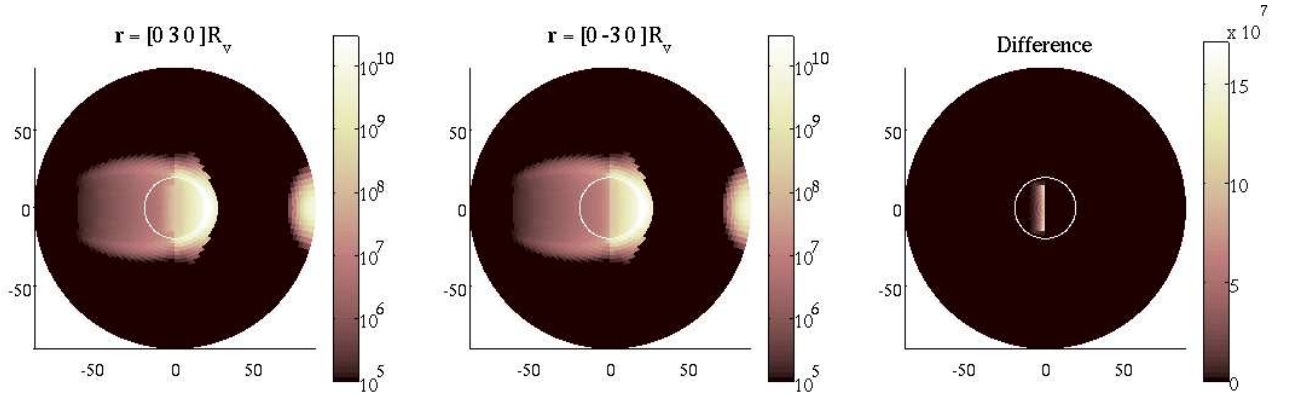


Fig. 7. ENA images from a vantage point at solar zenith angle  $\theta = 90^\circ$  located on the positive  $y$ -axis (left panel) and on the negative  $y$ -axis (middle panel). The right panel shows the difference between the left panel and the middle panel. The effect of the hydrogen bulge is seen as an increase in the ENA flux from the  $y > 0$  part of the nightside (left panel). The left and middle panels show ENA images on a logarithmic scale and the contribution from the bulge to the ENA images is relatively small.

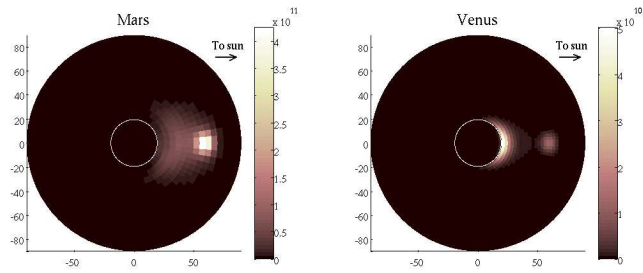


Fig. 8. ENA images from Mars (left) and Venus (right) from vantage points with solar zenith angles of  $120^\circ$  and planetocentric distance three radii of the respective planet. The image of the Martian environment (Gunell et al., 2004) is based on an MHD model of the plasma flow around Mars.

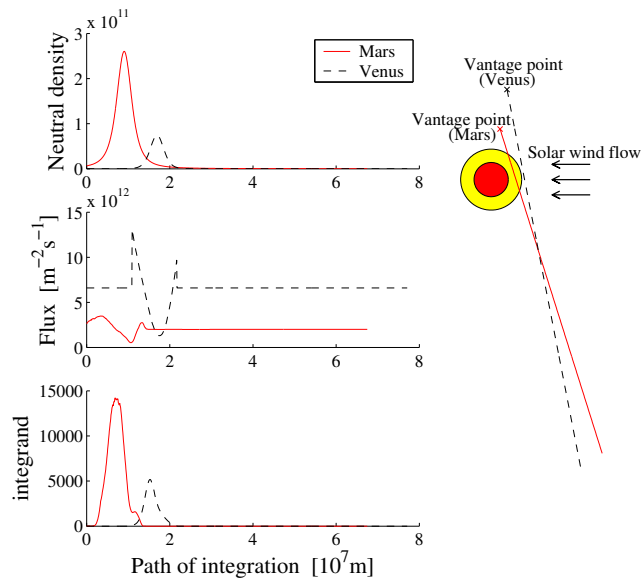


Fig. 9. The three panels on the left side show, from top to bottom, the total neutral gas density, the plasma flux, and the rate of ENA production in the direction toward the vantage point, as functions of distance along the line of sight from the vantage point. Solid and dashed lines represent values at Mars and Venus respectively. The ENA production rate, when integrated along the line of sight, gives the differential ENA flux that is shown in the ENA images. The right panel shows the lines of sight along for which the different quantities are plotted in the left panels. The filled red circle represents Mars and the yellow Venus. The paths of integration are counted from their respective vantage points, that are shown in the right panel.